

A Comprehensive Analysis of LNG as Coolant in Cooling Channel of Rocket Engine Under Supercritical Pressure Conditions

*Ibraheem Nasser**, *Chiara Manfletti*[†]*, *Tiziano Santese**, *Oskar Haidn**

** Chair of Space Propulsion and Mobility, Technical University of Munich, 85521 Ottobrunn, Germany*

ibrahem.nasser@tum.de – chiara.manfletti@tum.de

[†] Corresponding Author

Abstract

This study is focused on understanding the effect of impurities in LNG flow inside the cooling channels of rocket engines. LNG cooling systems' flow evolution and cooling capability are investigated numerically. The results show that to avoid two-phase flow in the cooling channel, the exit pressure from the cooling channel should be more than the critical pressure 4.6MPa for pure methane and more than the cricondenbar 5.1 and 7.5MPa for lean and rich LNG, respectively. The pressure drops decreased with increasing ethane, propane, and butane content. Cooling capabilities for pure methane and lean LNG are lower than for Rich LNG.

1. Introduction

Designers of liquid rocket engines have recently become increasingly interested in the potential use of methane as a denser and less expensive alternative to hydrogen in launch vehicles [1, 2] and a less expensive alternative to hazardous storable propellants for space propulsion [3]. Compared to other hydrocarbon fuels, methane has a higher specific impulse, superior cooling properties, and produces less soot deposition. Methane displays a unique behavior when used as a coolant with pressures above 50 bar. Methane enters the channels at supercritical pressure and subcritical temperatures. As the coolant picks up the heat, its temperature rises to and exceeds the critical value. Because the pressure and temperature of methane in cooling channels are so close to the critical point, the enormous fluctuations of thermal and transport properties that occur in the region around the critical point significantly impact how the coolant flows and how much heat is transferred. Analyzing the flow behavior and heat transfer characteristics in a thrust chamber cooled by regenerative cooling is experimentally complex. As a result, numerical simulations are frequently employed to investigate rocket cooling channels. The thermal behavior of cryogenic coolant fluids under transcritical conditions has been the subject of only a few experiments [4- 11]. The characteristics of methane under a high inflow temperature and an elevated single-sided heat load found in rocket nozzle cooling channels were studied by Heldens et al. [12]. They noticed that heat transfer is strongly influenced by the dynamic boundary layer development, which yields a steady growth in the Nusselt number. The behavior of methane flowing inside a cooling jacket which is demonstrated for the HYPROB program [13] cooling jacket, is described by Pizzarelli et al. [14] and Ricci et al. [15]. They studied the effects of different operating conditions and supported numerical methodologies to design LOX/Methane rocket engine cooling channels. The effects of mass flow rate, outlet pressure, surface roughness, and wall temperature on the thermal behavior of pure methane were analyzed by Shokri et al. [16]. The findings suggest that the inflection point in the density distribution of the coolant flow and differences in the slope of the transport property curves can be used as criteria for identifying the heat transfer deterioration and transcritical zones, respectively. Zhang et al. [17] studied the effect of artificial roughness with different rib heights and pitches. They found that the artificial roughness severely disturbs the flow field near the ribs. Moreover, the rib height was found to enhance heat transfer. A gradual temperature increase of the coolant near the hot wall manifested this effect. The impact of various aspect ratios and numbers of cooling channels on the gas-side Wall and coolant temperatures, as well as pressure drop, was investigated numerically by many researchers [11, 18, 19, 20, 21]. They found that the hot wall temperature can be significantly lowered without affecting the coolant pressure drop. Pizzarelli et al. [22] used data from numerical simulations to create a Nusselt number correlation that can represent the convective heat transfer properties of supercritical flow exhibiting deterioration. He used the Navier–Stokes equation's numerical solver developed in [23, 24] to collect heat-transfer data of supercritical methane in a heated tube for different pressure, temperature, and mass flux levels. Furthermore, it was found that increasing coolant pressure and surface roughness decreases the resultant wall temperature peak [25, 26].

Nomenclature	
C_p	specific heat, J/kg.K
D_h	hydraulic diameter, m
f	friction factor
h	heat transfer coefficient, W/m ² .K
H	height of the rectangular channel, m
k	thermal conductivity, W/m.K
L	length of test section, m
M	molar masses, g/mol
m	mass flow rate, kg/s
Nu	Nusselt number
p	pressure, Pa
P_c	critical pressure, Pa
q	heat flux, W/m ²
R	gas constant, 8.314 J/K.mol
T	temperature, K
T_c	the critical temperature, K
u	velocity, m/s
V	velocity
w	Speed of sound, m/s
\bar{x}	species mole fraction
x	x-axis, m
y	y-axis, m
y^+	dimensionless wall distance
z	z-axis, m
Greek symbols	
α	dimensionless form of the specific Helmholtz energy
δ	reduced mixture density
η	overall thermal-hydraulic performance
μ	viscosity, Pa.s
μ_t	turbulence viscosity
ρ	density, kg/m ³
τ	inverse reduced mixture temperature
$(\tau_{ij})_{eff}$	efficient deviatoric stress tensor
ω	the acentric factor
Subscripts	
b	bulk
cr	critical point
$cric$	cricondenbar
iw	Inner wall
i	x-coordinate
j	y-coordinate
m	mean
w	wall

In addition, a parametric analysis revealed the margins needed to meet specific wall temperature constraints [27]. The turbulent flow and heat transfer of supercritical methane in a helically coiled tube is studied by Gao et al. [28]. It was found that pressure and heat flux significantly affect the heat transfer of supercritical methane. The heat transfer deterioration in the cooling channels of liquid rocket engine occurs at a high heat flux level. A critical review is completed by Nasuti et al. [29]. He found that pressures significantly higher than the critical pressure [26] and increasing wall roughness [30, 31] can eliminate this undesired phenomenon. Gao et al. [32, 21] and Bai et al. [33] studied the heat transfer of supercritical methane in microchannel heat sinks with different geometric configurations. A numerical calculation showed an enhancement of heat transfer in wavy configurations. The thermophysical features of the coolant and how it transfers heat in heated channels directly influence a rocket engine's performance.

Fuels like hydrogen, methane, lean LNG, and rich LNG are potential coolant choices that theoretically make the system practical and satisfy performance requirements. For example, for a given operative pressure, hydrocarbons, which have a higher critical pressure than hydrogen, would be closer to the critical pressure than hydrogen and could flow in channels at a near-critical pressure. Such circumstances make thermophysical characteristics very variable, which may impact the fuels' ability to transport heat locally. Although impurities significantly affect heat transfer inside the rocket engine cooling channels [34, 35], only a minimal amount of work is available in the literature. A literature review shows a rocket engine's most current flow and heat transfer research is based on supercritical purified methane. However, the usage of this fluid in large quantities is not viable from an economic standpoint. Hence, the usage of LNG with rich hydrocarbon impurities is more realistic in the frame of space propulsion applications. There is a lack of research concerning the effects of impurities in cooling applications with supercritical fluids. The main objective of the current study is to compare how pure methane and its combinations behave when flowing through cooling channels. Two commercial LNG, which have about 97.5% and 88.7% mole fraction methane in a mixture including ethane, propane, butane, and nitrogen in various percentages for the remaining part, are selected in this study. Numerical studies analyze supercritical LNG's flow and heat transfer characteristics under different boundary conditions in a 2D circular cooling channel. The National Institute of Standards and Technology (NIST) [36, 37] database find the physical properties of purified methane and its mixtures. In addition, the database is implemented in Fluent by using a user-defined function. The species of impurities in LNG in the heating process are discussed. Moreover, heat transfer enhancement conditions are put forward in this research.

2. Thermophysical Property Models

LNG enters the cooling channel at supercritical pressure and subcritical temperature. Due to heat absorption, temperature evolves from subcritical to critical conditions. When a cooling fluid crosses the critical temperature, a pseudo-phase transition occurs, converting it from liquid to gas-like. The near-critical zone's thermodynamic and transport coolant properties also undergo significant changes. As a result, investigating state and transport property relations equations is the primary step in analyzing the coolant thermo-fluidic behavior in transcritical conditions.

2.1 Equation of State

GERG-2008 [38] seems the most accurate when dealing with hydrocarbons. It offers a wide validity range to cover both sub and supercritical conditions [39]. Since the cooling channel boundary conditions ensure pressures below 120 bar and temperatures of 600 K, this model is suitable for the present work. The GERG-2008 EOS is based on the Helmholtz free energy, a function with temperature pressure and mole fraction. The reduced Helmholtz free energy is divided into two parts. They represent the properties of the ideal-gas mixture and the residual part, respectively.

$$\alpha(\delta, \tau, \bar{x}) = \alpha^o(\rho, T, \bar{x}) + \alpha^r(\delta, \tau, \bar{x}) \quad (1)$$

$$\alpha^o(\rho, T, \bar{x}) = \sum_{i=1}^N x_i [\alpha_{oi}^o(\rho, T) + \ln x_i] \quad (2)$$

$$\alpha^r(\delta, \tau, \bar{x}) = \sum_{i=1}^N x_i \alpha_{oi}^r(\delta, T) + \sum_{i=1}^{N-1} \sum_{j=i+1}^N x_i x_j F_{ij} \alpha_{ij}^r(\delta, \tau) \quad (3)$$

The residual part is further subdivided into two additional terms. The first one represents the residual for every species separately, and the second computes the binary departure function for the mixture [40]. The reduced mixture density and the inverse reduced mixture temperature are calculated as

$$\delta = \frac{\rho}{\rho_r(\bar{x})} \quad (4)$$

$$\tau = \frac{T_r(\bar{x})}{T} \quad (5)$$

Where the density and temperature composition parameters are

$$\frac{1}{\rho_r(\bar{x})} = \sum_{i=1}^N x_i^2 \frac{1}{\rho_{c,i}} + \sum_{i=1}^{N-1} \sum_{j=i+1}^N 2x_i x_j \beta_{v,ij} \gamma_{v,ij} \frac{x_i + x_j}{\beta_{v,ij}^2 x_i + x_j} \frac{1}{8} \left(\frac{1}{\rho_{c,i}^{1/3}} + \frac{1}{\rho_{c,j}^{1/3}} \right)^3 \quad (6)$$

$$T_r(\bar{x}) = \sum_{i=1}^N x_i^2 T_{c,i} + \sum_{i=1}^{N-1} \sum_{j=i+1}^N 2x_i x_j \beta_{T,ij} \gamma_{T,ij} \frac{x_i + x_j}{\beta_{T,ij}^2 x_i + x_j} (T_{c,i} + T_{c,j})^{0.5} \quad (7)$$

The values of the binary parameters relating to species and other coefficients and the derivatives of the reduced Helmholtz free energy, the ideal-gas mixture, and residual parts concerning reduced temperature and density used in GERG-is 2008 can be founded in [38]. The thermophysical properties of a pure or mixture can be calculated by combining various derivatives of the reduced Helmholtz free energy parts. The pressure and isobaric heat capacity are calculated as follows.

$$\frac{P(\delta, \tau, \bar{x})}{\rho RT} = 1 + \delta \alpha_{\delta}^r \quad (8)$$

$$\frac{c_p(\delta, \tau, \bar{x})}{R} = -\tau^2 (\alpha_{\tau\tau}^o + \alpha_{\tau\tau}^r) + \frac{(1 + \delta \alpha_{\delta}^r - \delta \tau \alpha_{\delta\tau}^r)^2}{1 + 2\delta \alpha_{\delta}^r + \delta^2 \alpha_{\delta\delta}^r} \quad (9)$$

2.2 Transport Properties

The extended corresponding states (ECS) hypothesis is the most frequently used in literature to determine a mixture fluid's viscosity and thermal conductivity [37]. Mixture fluid dynamic viscosity and thermal conductivity are defined as a sum of dilute gas contribution, residual contribution, and critical contribution. And all the terms function with a mole fraction as below.

$$\mu = \mu^o(T, \bar{x}) + \mu^r(T, \rho, \bar{x}) + \mu^c(T, \rho, \bar{x}) \quad (10)$$

$$k = k^o(T, \bar{x}) + k^r(T, \rho, \bar{x}) + k^c(T, \rho, \bar{x}) \quad (11)$$

The dilute gas contribution is calculated with Lennard-Jones' potential for the mixture. The mixture method, pointed out by Gordon [41], calculates the dilute gas transport properties.

A Comprehensive Analysis of LNG as Coolant...

$$\mu^0(T, \bar{x}) = \sum_{i=1}^N x_i \mu_i^0 \left(x_i + \sum_{i=1, j \neq i}^N x_j \phi_{ij} \right)^{-1} \quad (12)$$

$$k^0(T, \bar{x}) = \sum_{i=1}^N x_i k_i^0 \left(x_i + \sum_{i=1, j \neq i}^N x_j \psi_{ij} \right)^{-1} \quad (13)$$

Where the equations of dilute gas part viscosity and thermal conductivity are pointed out for methane, ethane, propane, and butane [42] in equations (14-15) and for nitrogen [43] in equations (16-17), respectively, as follows:

$$\mu_i^0(T) = \frac{\left(\frac{5}{16}\right) \left(\frac{K_B}{1000\pi N_a}\right)^{0.5} (M_r T)^{0.5}}{\Omega \sigma_\mu^2} \quad (14)$$

$$k_i^0(T) = 1000 \mu_o (C_p^0 - 5R/2) [G_t(1) + G_t(2)\epsilon/kT] \quad (15)$$

$$\mu_i^0(T) = \sum_{i=1}^9 G_v(i) T^{(4-i)/3} \quad (16)$$

$$k_i^0(T) = \sum_{i=1}^9 G_t(i) T^{(4-i)/3} \quad (17)$$

Moreover, coefficients ϕ_{ij} and ψ_{ij} , which function with viscosity and molar weight of species, are defined as follows.

$$\phi_{ij} = \frac{1}{\sqrt{8}} \left[1 + \frac{W_i}{W_j} \right]^{-1/2} \left[1 + \left(\frac{\mu_i}{\mu_j} \right)^{1/2} \left(\frac{W_j}{W_i} \right)^{1/4} \right]^2 \quad (18)$$

$$\psi_{ij} = \phi_{ij} \left[1 + \frac{2.41(W_i - W_j)(W_i - 0.142W_j)}{(W_i + W_j)^2} \right] \quad (19)$$

The ECS approach is used to find the residual part contribution. For mixture calculation, nitrogen is employed as the reference fluid.

$$\mu^r(T, \rho, \bar{x}) = \mu_0^r(T_0, \rho_0) F_\mu^r \quad (20)$$

$$k^r(T, \rho, \bar{x}) = k_0^r(T_0, \rho_0) F_k^r \quad (21)$$

Species	CH ₄	C ₂ H ₆	C ₃ H ₈	C ₄ H ₁₀	N ₂
Pure	100	-	-	-	-
Lean	97.5	1.5	0.5	-	0.5
Rich	88.7	8	2	1	0.3

Table 1: Commercial grades of LPG methane (mole fraction %).

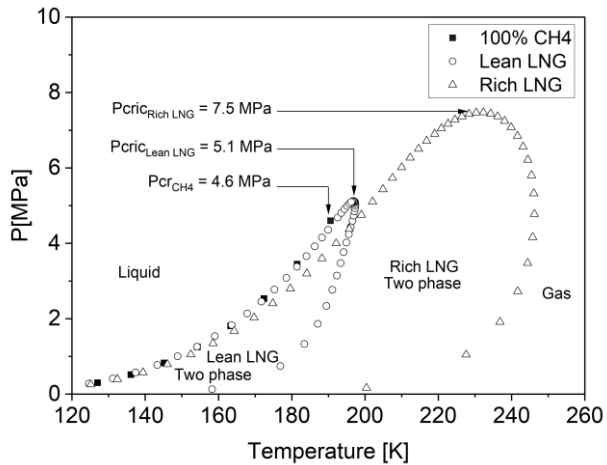


Figure 1: Vapor-liquid equilibrium of pure methane, lean and rich LNG.

Where the conformal temperature T_0 and density ρ_0 are calculated using the relationships

$$T_0 = \frac{T}{f_x} \text{ \& } \rho_0 = \rho h_x \quad (22)$$

Where the values of f_x and h_x that involve the individual pure fluid f_i and h_i are determined via mixing rules [37], the critical contribution part improves the thermal conductivity peak prediction near the critical point. It is assumed to equal zero for viscosity and evaluated according to the thermal conductivity model presented by Olchoway et al. [44]. This study analyzes pure methane as a coolant in the cooling channel and two different LNG. The first one (lean LNG) has a 97.5% methane mole fraction, and the other (Rich LNG) has an 88.7% methane mole fraction. Percentages for the remaining part are listed in Table 1. In addition, Fig. 1 presents their equilibrium vapor-liquid. It concludes that to avoid the two-phase flow in the cooling channel, the exit pressure from the cooling channel should be more than the critical pressure (4.6 MPa) for pure methane. For lean and rich LNG, the exit pressure should be more than the cricondenbar (5.1 and 7.5 MPa, respectively).

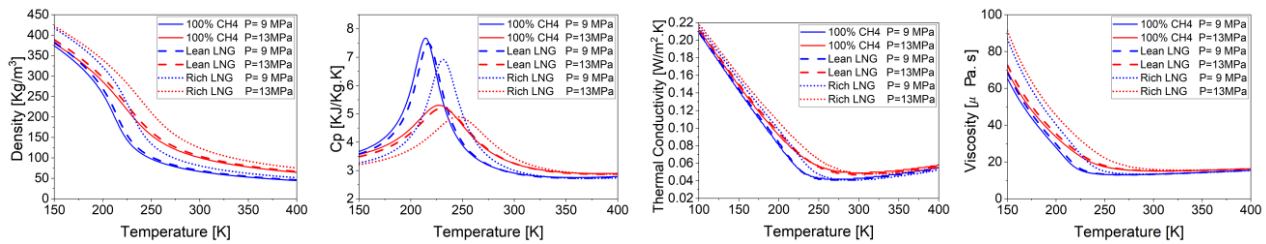


Figure 2: Thermophysical and transport properties of pure, lean, and rich LNG for three different pressures (9, 11, and 13 MPa) as a function of temperature. (a) Density, (b) Isobaric heat capacity, (c) Thermal conductivity, (d) Viscosity.

The calculated values for density, isobaric specific heat, viscosity, and thermal conductivity as a function of temperature and pressure, based on the selected state equation and transport property relations in the current study, are plotted. Fig. 2(a) and 2(b) show the density and isobaric heat capacity of pure, lean, and rich methane LNG for three different pressures (9, 11, and 13 MPa) as a function of temperature. Furthermore, Fig. 2(c) and 2(d) show the transport properties under the same conditions. A comparison with NIST data reveals a perfect agreement, validating the implementation of the correct thermophysical and transport properties.

3. Governing Equation

The governing Equation goes over the steady, compressible continuum equation. The flow must be modeled as compressible despite the low Mach number because the density of a supercritical natural gas undergoes dramatic changes [45]. The equations of mass, momentum, and energy conservation in cylindrical notation are solved in the CDF [46] as follows.

Mass Conservation

$$\frac{\partial}{\partial x}(\rho u_x) + \frac{1}{r} \frac{\partial}{\partial r}(\rho r u_r) = 0 \quad (23)$$

Momentum Conservation

$$\frac{\partial}{\partial x}(\rho u_x u_x) + \frac{1}{r} \frac{\partial}{\partial r}(\rho r u_x u_r) = -\frac{\partial p}{\partial x} + \frac{\partial \tau_{xx}}{\partial x} + \frac{1}{r} \frac{\partial}{\partial r}(r \tau_{xr}) \quad (24)$$

$$\frac{\partial}{\partial x}(\rho u_r u_x) + \frac{1}{r} \frac{\partial}{\partial r}(\rho r u_r u_r) = -\frac{\partial p}{\partial r} + \frac{\partial \tau_{rx}}{\partial x} + \frac{1}{r} \frac{\partial}{\partial r}(r \tau_{rr}) \quad (25)$$

Energy Conservation

$$\rho C_p u_x \frac{\partial T}{\partial x} + \rho C_p u_r \frac{\partial T}{\partial r} = \frac{\partial}{\partial x} \left(\lambda_t \frac{\partial T}{\partial x} \right) + \frac{1}{r} \frac{\partial}{\partial r} \left(r \lambda_t \frac{\partial T}{\partial r} \right) - \frac{T}{\rho} \left(\frac{\partial \rho}{\partial T} \right) \vec{u} \cdot \nabla p \quad (26)$$

The viscous terms are defined as

$$\tau_{xx} = \mu_{\text{eff}} \left[2 \frac{\partial u_x}{\partial x} - \frac{2}{3} (\nabla \cdot \mathbf{u}) \right] \quad (27)$$

$$\tau_{rr} = \mu_{\text{eff}} \left[2 \frac{\partial u_r}{r} - \frac{2}{3} (\nabla \cdot \mathbf{u}) \right] \quad (28)$$

$$\tau_{xr} = \tau_{rx} = \mu_{\text{eff}} \left[\frac{\partial u_x}{\partial r} + \frac{\partial u_r}{\partial x} \right] \quad (29)$$

$$\nabla \cdot (\mathbf{u}) = \frac{\partial u_x}{\partial x} + \frac{1}{r} \frac{\partial}{\partial r} (r u_r) \quad (30)$$

Equations variables are defined in the nomenclature. Although the Navier-Stokes equations accurately model turbulence, the required temporal and spatial resolutions necessitate massive computational resources. Consequently, except for the most straightforward low Reynolds number applications, the cost of Direct Numerical Simulation (DNS) of turbulence is prohibitively expensive [47, 48, 49, 50]. Another alternative is to use Large Eddy Simulation (LES), which directly computes only the largest turbulent scales and models the minor scales. Although this is viable for Reynolds numbers higher than those DNS can handle, it requires significant computation. The Reynolds-averaged Navier-Stokes (RANS) equations are the most widely used engineering approach. None of the turbulent scales is directly computed in this approach. The average effect of turbulence on the flow is modeled instead. In addition, one or more equations are added to the flow's governing equations. Previous numerical studies have demonstrated that the standard k- ϵ turbulence model [51] with an enhanced wall treatment in the near wall region can handle supercritical-pressure heat transfer of LNG under specific operating conditions. The Equation of the K- ϵ turbulence model is used to handle turbulent fluid flows follows.

$$\frac{\partial}{\partial x} (\rho u_x K) + \frac{1}{r} \frac{\partial}{\partial r} (r \rho u_x K) = \frac{\partial}{\partial x} \left[\left(\mu + \frac{\mu_t}{\sigma_k} \right) \frac{\partial K}{\partial x} \right] + \frac{1}{r} \frac{\partial}{\partial r} \left[\left(\mu + \frac{\mu_t}{\sigma_k} \right) \frac{\partial K}{\partial r} \right] - \rho \epsilon + G_k + G_b \quad (31)$$

$$\frac{\partial}{\partial x} (\rho u_x \epsilon) + \frac{1}{r} \frac{\partial}{\partial r} (r \rho u_x \epsilon) = \frac{\partial}{\partial x} \left[\left(\mu + \frac{\mu_t}{\sigma_\epsilon} \right) \frac{\partial \epsilon}{\partial x} \right] + \frac{1}{r} \frac{\partial}{\partial r} \left[\left(\mu + \frac{\mu_t}{\sigma_\epsilon} \right) \frac{\partial \epsilon}{\partial r} \right] + C_1 \frac{\epsilon}{k} (G_k + C_3 G_b) - C_2 \rho \frac{\epsilon^2}{k} \quad (32)$$

4. Test Case Description

4.1 Geometry Description and Boundary Conditions.

The present study uses a straight cooling channel with a circular cross-section. The length of the cooling channel is 40mm, and the diameter is 1mm. as shown in Fig.3. The imposed inlet pressure and temperature are 10MPa and 120K, respectively. Moreover, the mass flux is 10, 000 Kg/m². The outlet pressure is kept more than the cricondenbar pressure to avoid the two-phase region. The beginning unheated section with ten times diameter is employed to get a fully developed flow field before the heat transfer process. The unheated section with ten diameters at the end of the cooling channel is used to avoid the impacts of out-flow boundary conditions on the numerical results. Moreover, a constant heat flux of 8MW/m² is applied in the middle section. The absence of tangential turbulence transport can simplify the displayed geometry in Fig.3.

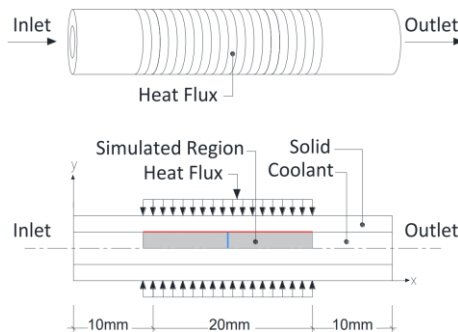


Figure 3: Schematic of the circular hollow regenerative cooling.

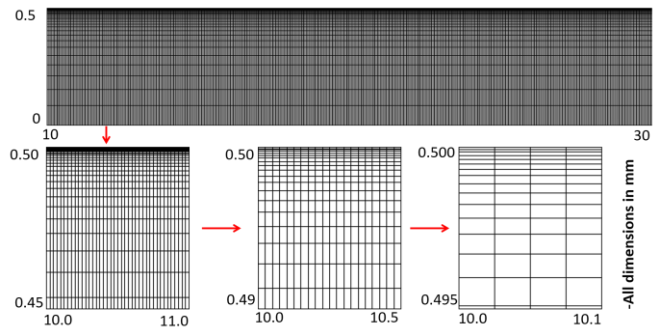


Figure 4: Schematic of the Computational mesh of the current study.

4.2. Grid convergence

A grid refinement examination has been accomplished for the channel, which has 40mm in length and 1mm in diameter. The number of cells of three different grids resolution is summarised in Table 2 for the test case geometry. It shows the stream-wise and vertical grid resolution in the three spatial directions. The same clustering principles produce the resolution for the various grids. For the course grid, the value of y^+ of a wall cell occurring for each grid is less than 2 and less than 1.0 for the medium and fine grid walls.

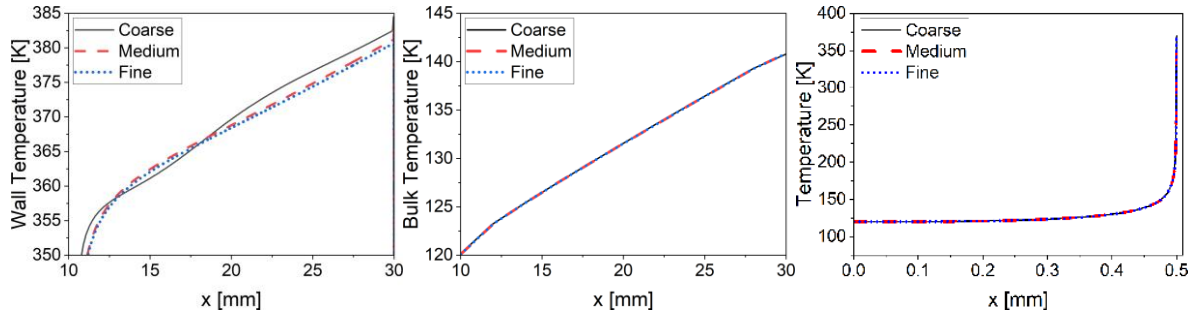


Figure 5: Mesh grid validation.

The evolution of the wall, bulk, and radial coolant temperatures of the cooling channel is shown in Fig.5 for the three grids. Temperature values demonstrate no impacts of the mesh on the result of bulk temperature are noticed. This is an anticipated result, indicating that the energy balance is perfectly correct, independent of the mesh resolution. However, the wall temperature has a visible displacement at various mesh levels. The results show a negligible difference between the fine and medium grids and a noticeable difference between the coarse and medium grids. As a result, the medium mesh, presented in Fig.4, has been chosen as the reference grid of this study.

LNG	Grid Size		y^+	No. of Element	Aspect Ratio	Mesh Growth Rate
	Radial	stream-wise				
Coarse	30	800	< 2	24,000	322.19	1.25
Medium	40	1600	< 1	64,000	367.19	1.20
Fine	50	3200	< 1	160,000	377.24	1.17

Table 2: Grid specifications for three different grids.

5. Validation

In this validation, experimental data [53] proposed by NASA were utilized to confirm that the model can predict heat transfer deterioration caused by increased heat flux under supercritical pressures. Pizzarelli et al. [54, 22] conducted a comparative study utilizing the same experimental data. The experimental investigations are for hydrogen flow in a heated pipe at sub and supercritical pressures and temperatures. According to [53], many experiments have been conducted. Test cases "0294", "0681", and "0706" have been selected for model validation. For test cases, the pipe's internal diameter is 8.51mm, and its length is 91.44 cm. The heat flux is applied to the last part of it. The heat flux distribution is reported in [54, 22], as shown in Fig. 6(a). For test "0294", the static pressure at the outlet is 4.92 MPa. And the inlet temperature is 42.4 K, where the mass flux is 734 (kg/m².s). For test "0681", the static pressure at the outlet, the inlet temperature, and the mass flux are 1.6 MPa, 26.8 K, and 1401 (kg/m².s), respectively. For test "0706", They are 4.95 MPa, 25.3 K, and 1385 (kg/m².s), respectively. The pressure and temperature of the coolant fluid inside the channel are in supercritical condition for the first test. For the second one, the temperature varies from a subcritical state to a supercritical state. The hydrogen flow in the pipe is axisymmetric and steady. The optimum mesh with the size of 50 × 3000 (Radial × stream-wise) is selected for simulation and clustered in the radial direction to reach y^+ less than 1.0. In Fig.6(b), a comparison study between the experimental data and numerical simulation. Numerical simulation using $k - \epsilon$ Enhanced wall treatment is presented for a wall temperature for case studies 0294, 0681, and 0706, respectively. The prediction of wall temperature agrees with experimental data. It can demonstrate that the $k - \epsilon$ turbulent model with enhanced wall treatment can be used confidently to explain the heat transfer deterioration in fluid flow near the critical region.

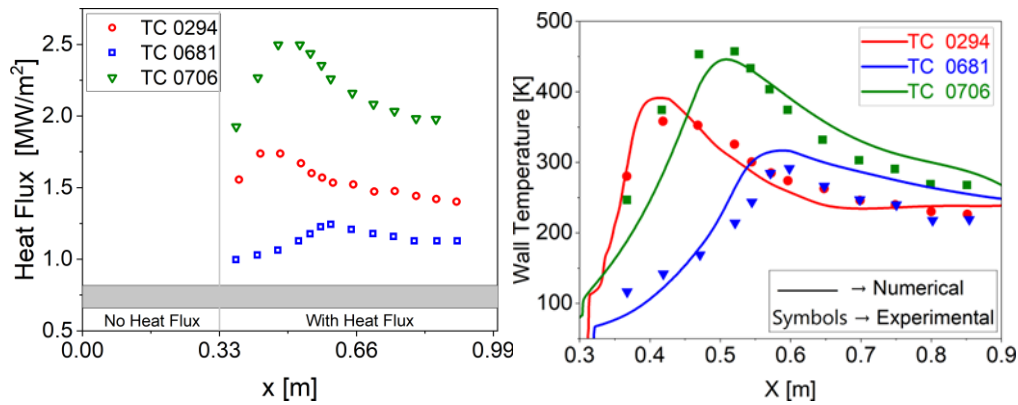


Figure 6: Comparison between the tube's experimental and numerical wall temperature following cryogenic. (a) Wall heat flux of experiments and (b) Wall temperature.

6. Result and discussion

6.1 Effect of LNG impurities

LNG flow in a straight channel with a circular cross-section is studied. Moreover, the impacts of different mole fractions of hydrocarbons are discussed in this section. The identical boundary conditions are operated for all cases to comprehend the impurities' effect on wall temperature and pressure drop. The contours of thermophysical and transport properties are displayed in Fig. 7. In this figure, the upper contour stands for pure methane, and the middle and lower contours stand to lean and rich LNG, respectively. The results indicate that the bulk density increases and the bulk isobaric heat capacity decrease along the channel as the percentage of hydrocarbon impurities increases in LNG. In addition, the bulk dynamic viscosity and thermal conductivity increase along the channel when the impurities mole fraction increases in LNG. The heated wall temperature and radial temperature profile at the center of the cooling channel, from the axis of symmetry to the wall, are presented in Fig. 8. The wall temperature in the case of rich LNG is higher than lean LNG and pure methane as the bulk isobaric heat capacity of pure methane is higher than that of lean, rich LNG. The isobaric heat capacity of pure methane is higher than the lean and rich LNG in the transcritical region. As a result, pure methane's bulk isobaric heat capacity has grown more than lean and rich LNG, as shown in Fig.10

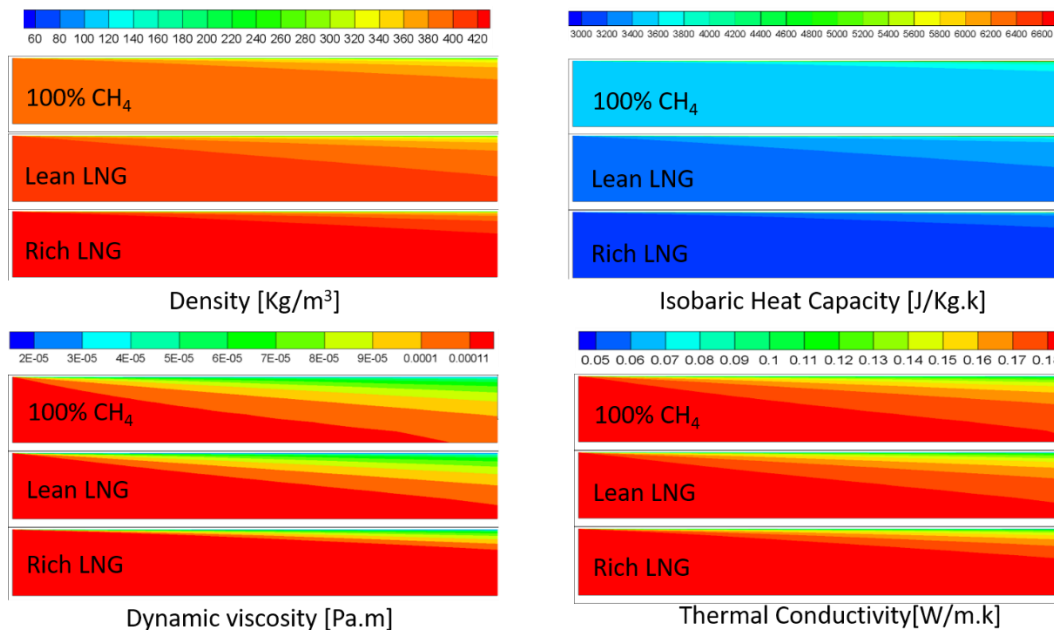


Figure 7: Comparison of flow properties contours for different LNG.

Furthermore, the radial temperature profiles are almost identical for three different LNG. However, there are some differences near the wall, as shown in Fig.8. Although these discrepancies amount to a small fraction of the temperature profile, they have a significant influence. For example, the bulk temperature of rich LNG increases by more than 1 K in a 1 cm cooling channel compared to pure methane. The Isobaric heat capacity of the coolant close to the wall is negligible, as shown in Fig.10. However, a peak in specific heat capacity is displayed near the wall. After this extreme point, the heat capacity abruptly decreases until it stabilizes at a relatively consistent behavior, as shown in Fig. 10. This phenomenon occurred because the coolant crossed the Widom line from gas-like to liquid-like. As a result, the turbulence near the wall should be increased by increasing the roughness or using a ribbed to maximize the isobaric heat capacity close to the wall and minimize the wall temperature.

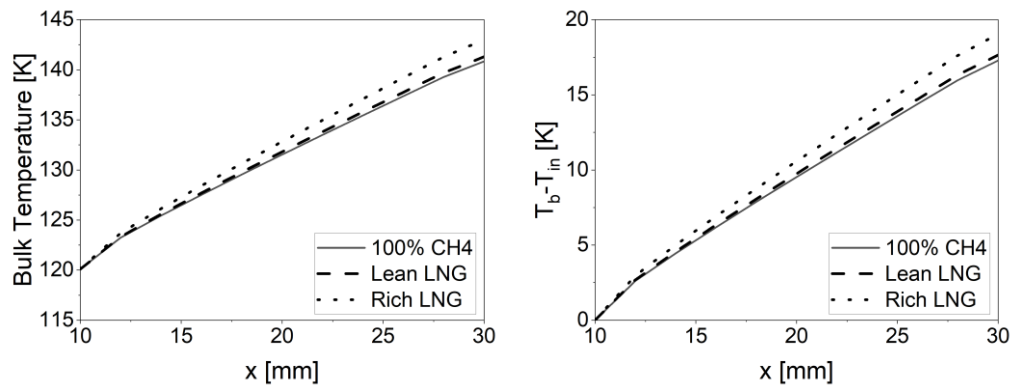


Figure 8 : (a) Bulk Temperature and (b) Bulk Temperature drop along the cooling channel for different LNG.

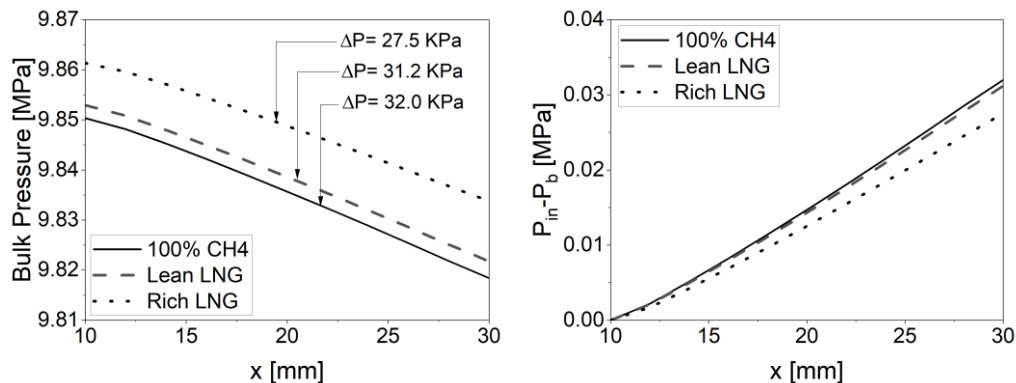


Figure 9 : (a) Bulk pressure and (b) Bulk pressure drop along the cooling channel for different LNG.

A comprehensive study is conducted to investigate the effect of hydrocarbon impurities on a pressure drop in a cooling channel. It found that the bulk pressure of pure methane is slight. The pressure drop becomes high because pure methane is lighter than lean and rich LNG, as shown in Fig.9. The bulk density drop is almost similar for different LNG. The density near the wall is small and then increases rapidly, as shown in Fig.11. The pressure drop of denser LNG is small compared to light LNG at the same mass flow rate because the coolant velocity decreases for denser LNG.

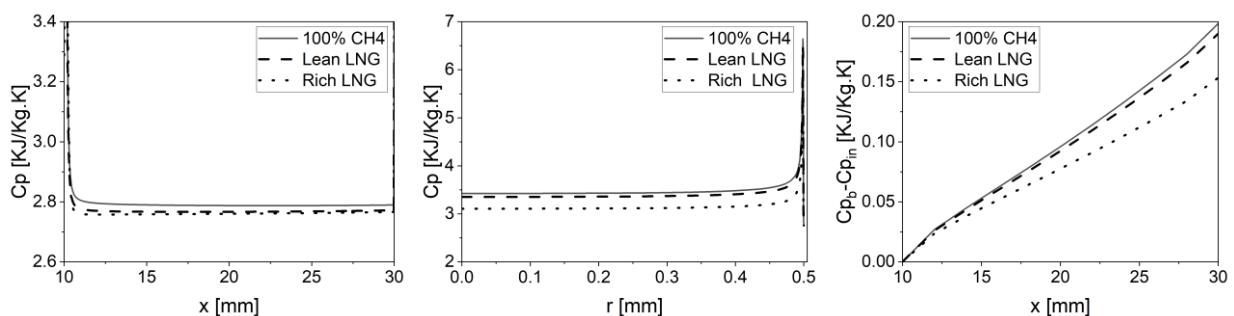


Figure 10: Isobaric heat capacity profile. (a) Along the heated wall, (b) Radial at $x/D=20$ and (c) bulk Isobaric heat capacity variation along the cooling channel for different LNG.

A Comprehensive Analysis of LNG as Coolant...

Pure methane's bulk thermal conductivity and dynamic viscosity are smaller than the lean and rich LNG in the cooling channel. Moreover, the drop of the total bulk thermal conductivity concerning the inlet total thermal conductivity is identical for different LNG. The decline of the bulk total dynamic viscosity concerning the inlet total dynamic viscosity grew faster for rich LNG thermal conductivity, and dynamic viscosity near the wall is small and then increased rapidly, as shown in Fig. 12 and Fig. 13. Overall, the transport properties increase with more hydrocarbon impurities.

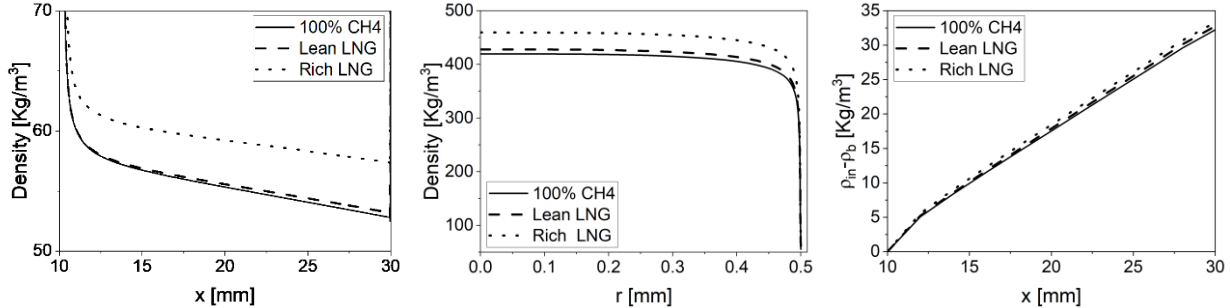


Figure 11: Density profile. (a) Along the heated wall, (b) Radial at $x/D=20$ and (c) bulk Density variation along the cooling channel for different LNG.

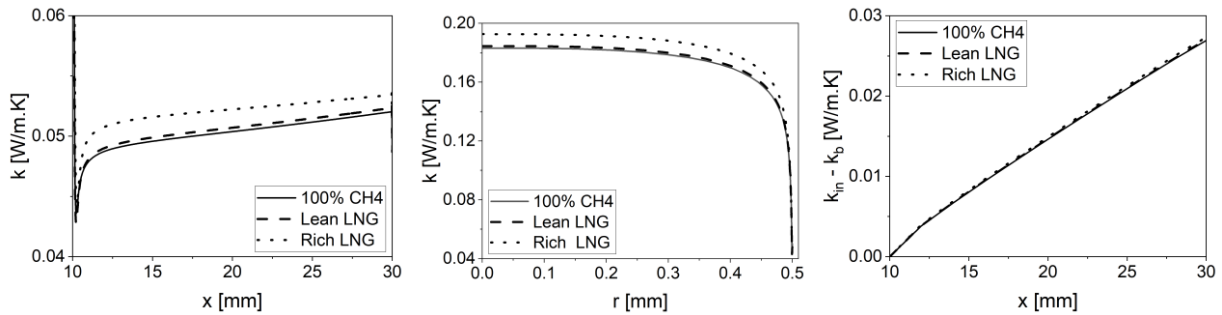


Figure 12: Thermal conductivity profile. (a) Along the heated wall, (b) Radial at $x/D=20$ and (c) bulk Thermal conductivity variation along the cooling channel for different LNG.

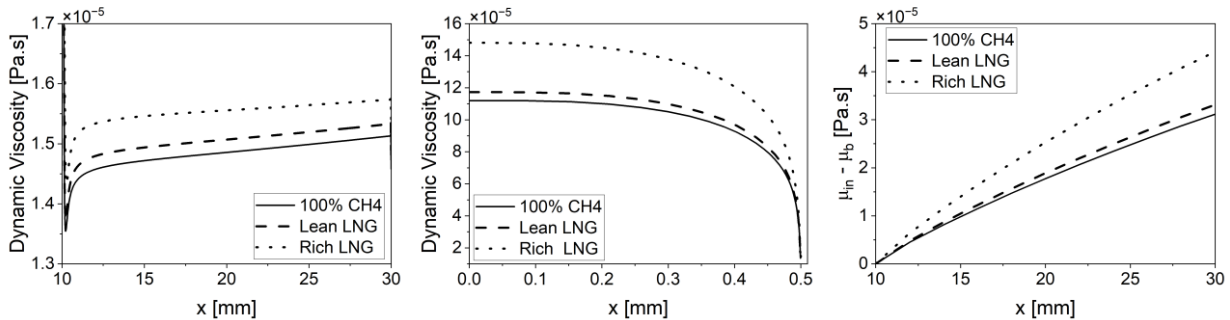


Figure 13: Dynamic Viscosity profile. (a) Along the heated wall, (b) Radial at $x/D=20$ and (c) bulk Dynamic Viscosity variation along the cooling channel for different LNG.

6.2 Effect of ethane, propane, and butane impurities

Binary mixtures of methane–ethane, methane–propane, and methane–butane have been evaluated and presented in this section. Throughout this study, the percentage of ethane, propane, or butane mole fraction is 0, 25, 50, 75, and 100%; the remaining amount is methane. The Vapor–liquid equilibrium of mixtures is presented in Fig.14. The cricondenbar pressures of the mixture are more than the critical pressure of pure methane and ethane. It is 6.73 and 6.75 MPa for the mixture has 25% and 50% mole fraction of ethane, respectively. Moreover, it decreases to 5.96 MPa for a mixture of 75% ethane. as shown in Fig. 14(a). The max cricondenbar pressure is 9.9 MPa for a mixture with a 25% mole fraction of propane. Moreover, it decreases to 8.61 and 6.48 MPa for the mixture with 50% and 75% mole fractions of propane, respectively, as illustrated in Fig.14(b). In addition, the maximum cricondenbar pressure is 14.43 MPa for a mixture with a 25% mole fraction of butane. Thus, it is more than three times methane's critical pressure, as shown in Fig. 14(c).

As a result of that, designers should raise the exit pressure of the cooling channel to avoid the two-phase region by at least 2 MPa for the methane-ethane mixture compared with the minimum exit pressure of pure methane or ethane. The exit pressure should keep more than 9.9 MPa for the methane-propane mixture. It means the operating pressure should increase by more than 54 bar compared with the minimum operating pressure of pure methane. In the case of the methane-butane mixture, more than 14.43 MPa should remain the exit pressure, increasing the operating pressure to 100 bar compared to the minimum operating pressure of pure methane. Hydrocarbon impurities in liquefied natural gas significantly impact rocket engine operating pressure conditions. It can lead to the occurrence of a two-phase flow. High-purity fuel use can minimize these issues and ensure optimal rocket engine performance. In this analysis, the boundary conditions for the methane-ethane mixture are kept as in the previous section. The inlet conditions become 14 MPa and 250K for methane-propane simulation, increasing to 16 MPa and 250K for the methane-butane cases to avoid two-phase flow.

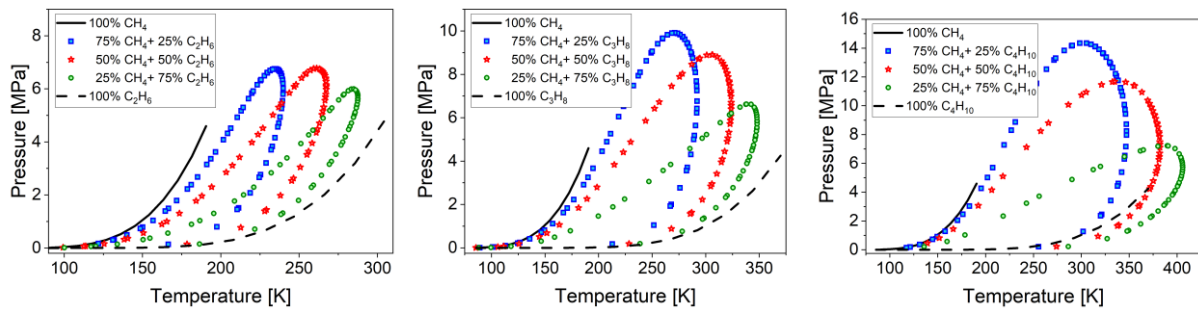


Figure 14: Vapor-liquid equilibrium of (a) methane-ethane mixture, (a) methane-propane mixture, and (a) methane-butane mixture.

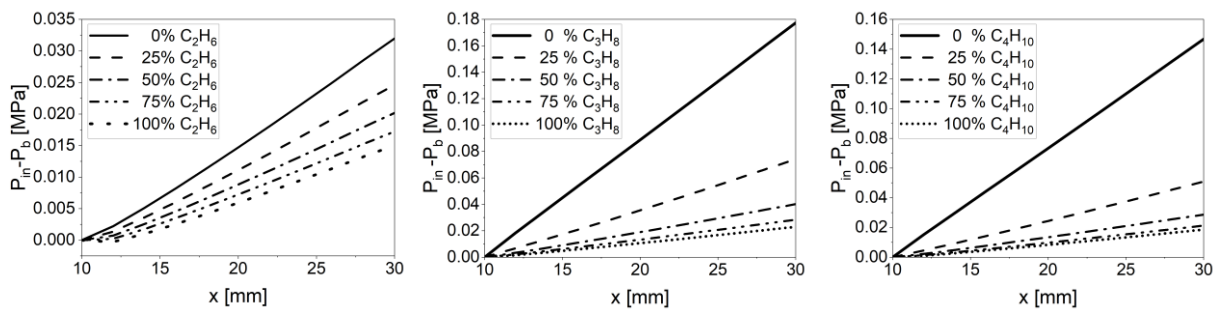


Figure 15 : bulk pressure drop for different mole fractions of (a) ethane, (b) propane, and (c) butane.

The percentage of hydrocarbon mole fraction has a scientific effect on the pressure drop of the coolant channel. However, it decreases with increasing hydrocarbon mole fraction, as shown in Fig.15. This phenomenon occurs because the coolant becomes denser with more hydrocarbon mole fraction. The coolant velocity decreases for specific mass flow rate and the bulk pressure increases. It concludes that a lower mole fraction of ethane generates a more significant pressure drop. The wall temperatures are displayed in Fig.16. They increase with the hydrocarbon mole fraction. The rate of increasing temperature decreases with increasing the mole fraction of hydrocarbons.

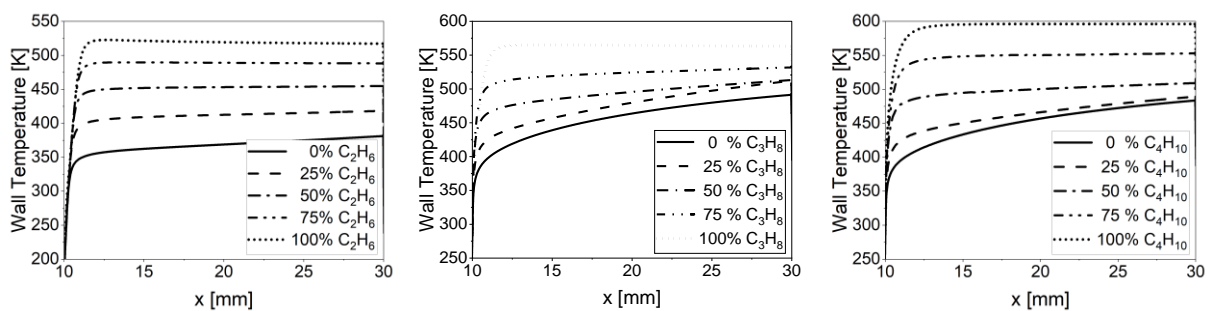


Figure 16 : Wall temperature variation for different mole fractions of (a) ethane, (b) propane, and (c) butane.

The density, pressure drop, velocity, and isobaric heat capacity contours are presented for methane-ethane, methane-propane, and methane-butane in Fig. 17-19, respectively. These impurities can have a significant impact on the properties of the fluid in the cooling channel. The presence of hydrocarbon impurities can change the density of the fluid in the

A Comprehensive Analysis of LNG as Coolant...

cooling channel. This change can affect the heat transfer properties and lead to changes in the temperature gradients. The pressure drop along the cooling channel is affected by the presence of hydrocarbon impurities. The flow resistance decreases, leading to a lower pressure drop, affecting the cooling system's overall efficiency. The presence of hydrocarbon impurities can impact the velocity of the fluid. Changes in fluid velocity led to changes in the Reynolds number, affecting the onset of turbulent flow. In addition, it affects the specific heat capacity of the fluid. It changes the heat the fluid absorbs during the cooling process. Hydrocarbon impurities can significantly impact the fluid's properties in a rocket engine cooling channel using LNG as a coolant. Considering these factors when designing such cooling systems is essential to ensure proper heat transfer and efficiency.

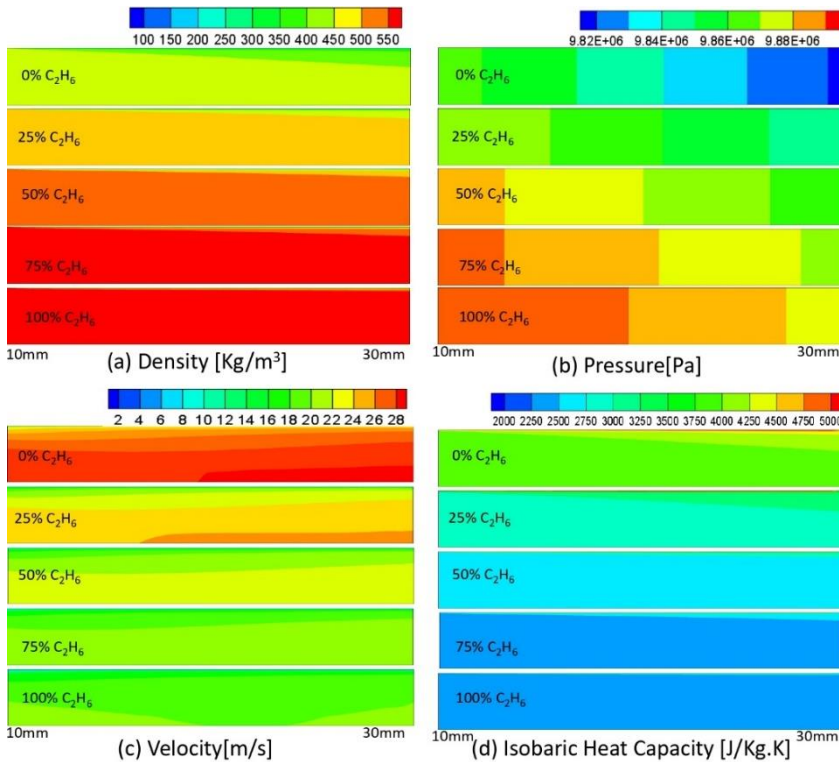


Figure 17 : Comparison of flow properties contours for different ethane mole fractions.

7. Conclusion

A literature survey demonstrated that most previous numerical investigations have concentrated on pure methane as a coolant inside the rocket engine cooling channel. In contrast, the rocket engine cooling channels are generally cooled using LNG with many impurities. In addition, it significantly affects the thermophysical and transport properties of the coolant along the cooling channel, especially in near-critical conditions. Moreover, it affects the cooling channel's wall temperature and pressure drop. The main objective of the present study was to understand the effects of hydrocarbon impurities on methane flow under the same parameters inside the heated straight cooling channel. The real gas state equations, the transport property relations of the mixture, were defined as a user-defined function to calculate the thermophysical and transport properties. The turbulence model was validated with experimental data.

Hydrocarbon impurities in liquefied natural gas can significantly impact cooling capabilities and pressure drop in a rocket engine cooling system operating under supercritical conditions. Using supercritical fluids as coolants increases the heat transfer capability of the coolant, allowing for more efficient cooling and better engine performance. However, the presence of hydrocarbon impurities in the LNG used as a coolant can significantly affect the cooling capabilities of the engine. These impurities have a significant effect on thermophysical and transport properties, leading to an effect on operating conditions and reducing heat transfer efficiency and pressure drop.

In summary, the impact of hydrocarbon impurities in LNG on the cooling capabilities and pressure drop in rocket engine cooling under supercritical conditions can be significant. Appropriate measures must be taken to remove or stabilize these impurities to ensure optimal engine performance.

Funding

The work was partly financed by the technology program MATRIKSTOSCA by the German Space Agency, DLR, Bonn, under contract No. 50RL2115.

Figure 18 : Comparison of flow properties contours for different propane mole fractions.

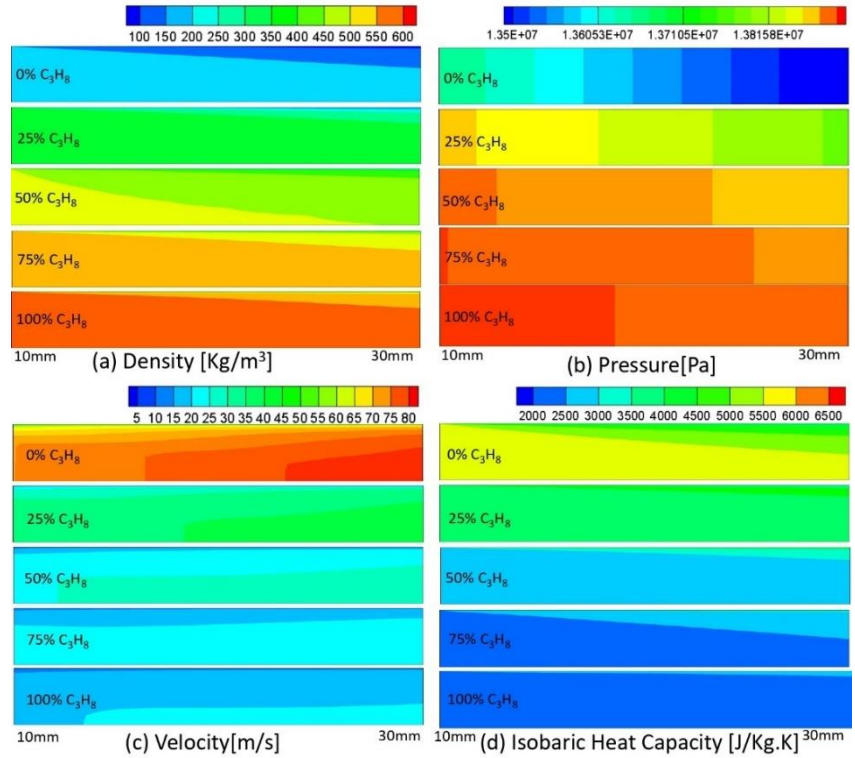
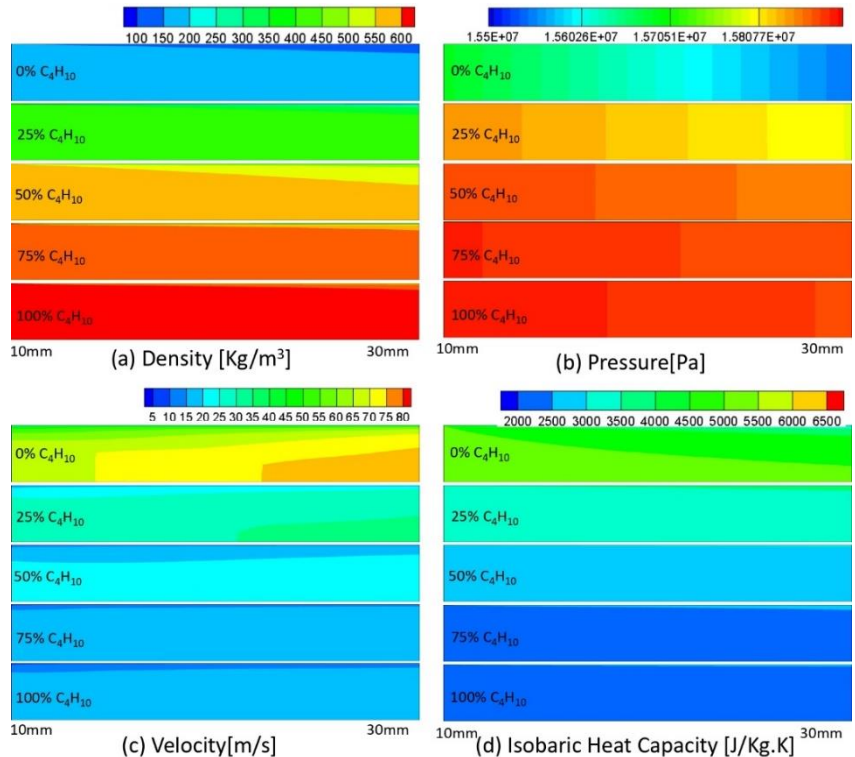


Figure 19 : Comparison of flow properties contours for different butane mole fractions.



References

- [1] R. Schuff, M. Maier, O. Sindiy, C. Ulrich, S. Fugger. 2006. Integrated modeling and analysis for a Lox/Methane expander cycle engine: Focusing on regenerative cooling jacket design. In: *42nd AIAA/ASME/SAE/ASEE Joint Propulsion Conference Exhibit*.
- [2] C. D. Brown. 2004. Conceptual investigations for a methane-fueled expander rocket engine. In: *40th AIAA/ASME/SAE/ASEE Joint Propulsion Conference and Exhibit*.

- [3] Y. Hong, Z. Liu, S. Silvestri, M. P. Celano, O. J. Haidn, Z. Yu. 2019. An experimental and modeling study of heat loads on a subscale methane rocket motor. *Acta Astronautica*. 164:112–120
- [4] R. Votta, F. Battista, V. Salvatore, M. Pizzarelli, G. Leccese, F. Nasuti, S. Meyer. 2016. Experimental investigation of trans critical methane flow in rocket engine cooling channel. *Applied Thermal Engineering*. 101:61–70.
- [5] R. Votta, F. Battista, A. Gianvito, A. Smoraldi, V. Salvatore, M. Pizzarelli, G. Leccese, F. Nasuti, S. Shark, R. T. Feddema, S. E. Meyer. 2014. Experimental investigation of methane in transcritical conditions. In: *50th AIAA/ASME/SAE/ASEE Joint Propulsion Conference*.
- [6] A. Trejo, A. G. Trujillo, M. Galvan, A. R. Choudhuri, J. C. Melcher, J. J. Bruggemann. 2014. Experimental investigation of liquid methane convection and boiling in rocket engine cooling channels. In: *50th AIAA/ASME/SAE/ASEE Joint Propulsion Conference*.
- [7] A. Trejo, A. G. Trujillo, M. Galvan, A. R. Choudhuri, J. C. Melcher, J. J. Bruggemann. 2016. Experimental investigation of methane convection and boiling in rocket engine cooling channels. *Journal of Thermophysics and Heat Transfer*. 30:937–945.
- [8] D. Ricci, P. Natale, F. Battista. 2016. Experimental and numerical investigation on the behavior of methane in supercritical conditions. *Applied Thermal Engineering*. 107:1334–1353.
- [9] B. Liu, Y. Zhu, J.J. Yan, Y. Lei, B. Zhang, P.X. Jiang, Experimental investigation of convection heat transfer of n-decane at supercritical pressures in small vertical tubes. 2015. *International Journal of Heat and Mass Transfer*. 91:734–746.
- [10] J. Haemisch, D. Suslov, M. Oswald. 2019. Experimental study of methane heat transfer deterioration in a subscale combustion chamber. *Journal of Propulsion and Power*. 35
- [11] J. Haemisch, D. Suslov, M. Oswald. 2021. Experimental and numerical investigation of heat transfer processes in rocket engine cooling channels operated with cryogenic hydrogen and methane at supercritical conditions. *Transactions of the Japan Society for Aeronautical and Space Sciences. Aerospace Technology Japan*. 19:96–105.
- [12] J. C. Heldens, J. Fridh, J. Ostlund. 2021. On the characterization of methane in rocket nozzle cooling channels. *Acta Astronautica*. 186:337–346
- [13] V. Salvatore, F. Battista, R. Votta, M. d. Clemente, M. Ferraiuolo, P. Roncioni, D. Ricci, P. Natale, M. Panelli, D. Cardillo, P. D. Matteis. 2012. Design and development of a LOX/LCH4 technology demonstrator. In: *48th AIAA/ASME/SAE/ASEE Joint Propulsion Conference & Exhibit*.
- [14] M. Pizzarelli, B. Betti, F. Nasuti, D. Ricci, P. Roncioni, F. Battista, V. Salvatore. 2014. Cooling channel analysis of LOX/LCH4 rocket engine demonstrator. In: *Joint Propulsion Conference*.
- [15] D. Ricci, F. Battista, M. Fragiaco. 2022. Transcritical behavior of methane in the cooling jacket of a liquid-oxygen/liquid-methane rocket-engine demonstrator. *Energies*. 15:4190.
- [16] M. Shokri, A. Ebrahimi, Heat transfer aspects of regenerative cooling in methane-based propulsion systems. 2018. *Aerospace Science and Technology*. 82: 412-424
- [17] M. Zhang, B. Sun, Effect of artificial roughness on flow and heat transfer of trans critical methane. 2020. *International Journal of Thermal Sciences*. 158:106528.
- [18] A. Ulas, E. Boysan. Numerical analysis of regenerative cooling in liquid propellant rocket engines. 2013. *Aerospace Science and Technology*. 24:187–197.
- [19] M. Pizzarelli, F. Nasuti, M. Onofri. 2014. Effect of cooling channel aspect ratio on rocket thermal behavior, *Journal of Thermophysics and Heat Transfer*. 28:410–416.
- [20] M. Pizzarelli, F. Nasuti, M. Onofri. 2013. Trade-off analysis of high aspect ratio cooling channels for rocket engines, *International Journal of Heat and Fluid Flow*. 44:458–467.
- [21] Z. Gao, T. Wang, Y. Yang, X. Shang, J. Bai, P. Li. 2022. Heat transfer analysis of supercritical methane in microchannels with different geometric configurations on high power electromechanical actuator. *Journal of Electronic Packaging*. 144:041014.
- [22] M. Pizzarelli. 2016. A CFD-derived correlation for methane heat transfer deterioration. *Numerical Heat Transfer, Part A: Applications* 69:242–264.
- [23] M. Pizzarelli, R. Paciorri, F. Nasuti, M. Onofri, C. Merkle, S. Rebay. 2009. Numerical analysis of three-dimensional flow of supercritical fluid in cooling channels. *AIAA Journal*. 47:2534–2543.
- [24] M. Pizzarelli, F. Nasuti, M. Onofri. 2013. Coupled wall heat conduction and coolant flow analysis for liquid rocket engines. *Journal of Propulsion and Power*. 29:34–41.
- [25] M. Pizzarelli, F. Nasuti, M. Onofri, P. Roncioni, R. Votta. 2015. F. Battista, Heat transfer modeling for supercritical methane flowing in rocket engine cooling channels. *Applied Thermal Engineering*. 75:600–607.
- [26] B. Ruan, W. Lin. 2022. Numerical investigation on heat transfer and flow characteristics of supercritical methane in a horizontal tube. *Cryogenics*. 124:103482.
- [27] M. Leonardi, M. Pizzarelli, F. Nasuti. 2019. Analysis of thermal stratification impact on the design of cooling channels for liquid rocket engines. *International Journal of Heat and Mass Transfer*. 135:811–821.
- [28] Z. Gao, J. Bai, J. Zhou, C. Wang, P. Li. 2020. Numerical investigation of supercritical methane in helically coiled tube on regenerative cooling of liquid rocket electromechanical actuator. *Cryogenics*. 106:103023.

- [29] F. Nasuti, M. Pizzarelli. 2021. Pseudo-boiling and heat transfer deterioration while heating supercritical liquid rocket engine propellants. *The Journal of Supercritical Fluids*. 168:105066
- [30] K. Xu, L. Tang, H. Meng. 2015. Numerical study of supercritical-pressure fluid flows and heat transfer of methane in ribbed cooling tubes. *International Journal of Heat and Mass Transfer*. 84:346–358.
- [31] B. Latini, M. Fiore, F. Nasuti. 2022. Modeling liquid rocket engine coolant flow and heat transfer in high roughness channels. *Aerospace Science and Technology*. 126:107672.
- [32] Z. Gao, T. Wang, J. Bai, Z. Wang, K. Qiao, P. Li. 2022. Thermal performance investigation of supercritical methane in mini channel heat sink on flight vehicle actuator under geometry effect of cross-section. *Numerical Heat Transfer, Part A: Applications*. 1–16.
- [33] J. Bai, J. Pan, X. He, K. Wang, L. Tang, R. Yang. 2020. Numerical investigation on thermal-hydraulic performance of supercritical LNG in sinusoidal wavy channel based printed circuit vaporizer. *Applied Thermal Engineering* 175:115379.
- [34] A. Urbano, F. Nasuti. 2013. Numerical study of liquefied natural gas as a coolant in liquid rocket engines, Proceedings of the Institution of Mechanical Engineers, Part G: *Journal of Aerospace Engineering*. 227:1130 – 1143.
- [35] A. Urbano, F. Nasuti. 2014. Parametric analysis of cooling properties of candidate expander-cycle fuels. *Journal of Propulsion and Power*. 30:153–163.
- [36] P. Linstrom: 1997. NIST chemistry webbook. *NIST standard reference database*.
- [37] M. L. Huber, E. W. Lemmon, I. H. Bell, M. O. McLinden. 2020. The NIST ref prop database for highly accurate properties of industrially important fluids. *Industrial Engineering Chemistry Research* 61:15449– 15472.
- [38] O. Kunz, W. Wagner. 2012. The gerg-2008 wide-range Equation of state for natural gases and other mixtures: an expansion of GERG-2004. *Journal of chemical engineering data*. 57:3032–3091.
- [39] F. Varzandeh, E. H. Stenby, W.d. Yan. 2017. Comparison of GERG-2008 and simpler EOS models in calculation of phase equilibrium and physical properties of natural gas-related systems. *Fluid Phase Equilibria*. 43:21–43.
- [40] D. Rowland, T. J. Hughes, E. F. May. 2016. Extending the gerg-2008 Equation of state: Improved departure function and interaction parameters for (methane + butane). *The Journal of Chemical Thermodynamics*. 97:206–213.
- [41] S. Gordon. 1994. Computer program for calculation of complex chemical equilibrium compositions and applications. *Springfield*.
- [42] B. A. Younglove, J. F. Ely. 1987. Thermophysical properties of fluids. ii. methane, ethane, propane, isobutane, and normal butane. *Journal of Physical and Chemical Reference Data*. 16:577–798.
- [43] B. Younglove. 1982. Thermophysical properties of fluids: Argon, ethylene, parahydrogen, nitrogen, nitrogen trifluoride, and oxygen. *Journal of Physical and Chemical Reference Data* .11.
- [44] G. A. Olchowy, J. V. Sengers. 1989. A simplified representation for the thermal conductivity of fluids in the critical region. *International Journal of Thermophysics*. 10:417–426.
- [45] J. Jiang, J. M. Prausnitz. 2000. Critical temperatures and pressures for hydrocarbon mixtures from an equation of state with renormalization- group theory corrections. *Fluid Phase Equilibria*. 169:127–147.
- [46] P. R. M. R. S. V. Anderson D., Tannehill J.C. 2020. Computational Fluid Mechanics and Heat Transfer, 4th Edition *Springer*.
- [47] J. H. Ferziger, M. Peri'c, R. L. Street. 2002. Computational methods for fluid dynamics, Vol. 3. *Springer*.
- [48] J. H. Bae, J. Y. Yoo, H. Choi. 2005. Direct numerical simulation of turbulent supercritical flows with heat transfer, *Physics of Fluids*. 17:105104.
- [49] F. Nasuti, A. Torricelli, S. Pirozzoli. 2021. Conjugate heat transfer analysis of rectangular cooling channels using modeled and direct numerical simulation of turbulence. *International Journal of Heat and Mass Transfer* 181:121849.
- [50] P. Orlandi, D. Sassun, S. Leonardi. 2016. DNS of conjugate heat transfer in presence of rough surfaces, *International Journal of Heat and Mass Transfer*. 100:250–266
- [51] S. H. El-Tahry. 1983. K-epsilon Equation for compressible reciprocating engine flows. *J. Energy*. 7:345–353.
- [52] M. Wolfshtein. 1969. The velocity and temperature distribution in one- dimensional flow with turbulence augmentation and pressure gradient, *International Journal of Heat and Mass Transfer*. 12:301–318.
- [53] R. Friedman, R. W. Graham, R. C. Hendricks, Y. Y. Hsu. 1966. Experimental heat-transfer results for cryogenic hydrogen flowing in tubes at subcritical and supercritical pressures to 800 pounds per square inch absolute. *NASA-TN-D-3095*.
- [54] M. Pizzarelli, A. Urbano, F. Nasuti. 2010. Numerical analysis of deterioration in heat transfer to near-critical rocket propellants, *Numerical Heat Transfer. Part A: Applications*. 57:297–314.